A Bayesian Approach to Device-free Localization: Modeling and Experimental Assessment

Stefano Savazzi[1], Monica Nicoli[2], Francesca Carminati[2], Michele Riva[2]
[1]National Research Council of Italy (CNR), IEIIT institute, Milano, [2]DEIB, Politecnico di Milano,
E-mail: stefano.savazzi@cnr.it, monica.nicoli@polimi.it,

***Abstract*— Device-free positioning allows to localize and track passive targets (i.e., not carrying any electronic device) moving in an area monitored by a dense network of low-power and battery-operated wireless sensors. The technology is promising for a wide number of applications ranging from ambient intelligence in smart spaces, intrusion detection, emergency and rescue operations in critical areas. In this paper, a new approach is proposed where *both* the average path-loss *and* the degree of fluctuation of the received signal strength induced by the target movement are jointly modeled based on the theory of diffraction. A novel stochastic model is derived and used for the evaluation of fundamental performance limits. The model is proved to be tight enough to be adopted for real-time estimation of the target location. The proposed localization system is validated by extensive experimental studies in both indoor and outdoor environments, dealing with model calibration in practical scenarios and comparing the performance of different Bayesian methods for online localization. The test-bed system allows for efficient and flexible target tracking without requiring any action from the end-users. In addition, the technology is proven to be readily applicable over the existing IEEE 802.15.4 compliant PHY layer standard by adapting the low-level MAC firmware.**

I. Introduction

The widespread adoption of wireless technologies in several contexts and environments has fostered the interest in radio localization systems to support new location-aware applications. Most of the research in wireless positioning has focused on device-based active localization, where a wireless device is attached to the tracked entity and actively participates in the localization process [1]. In contrast to active solutions, device-free passive localization [2] is an emerging approach for tracking objects or people moving in areas covered by a wireless communication network. In device-free localization, the tracked entity - a person, an object, or an aggregate of persons/objects - is neither required to carry devices nor to take an active part in the positioning process. The system relies on the fact that the signals received by the radio devices are affected by the presence of a moving entity obstructing the radio propagation in the surrounding area, so it is possible to locate the target by using radio imaging techniques [3]. As depicted in Fig. 1, a moving target traversing a link causes perturbations of the received signal strength (RSS). Measuring the induced RSS fluctuations at multiple points over the space allows to reconstruct an image of the area and locate the moving object. Device-free localization is promising for a wide number of applications ranging from context awareness in mobile computing, ambient assisted living in smart spaces, intrusion detection, emergency and rescue operations in hazardous areas, access control and counting, pedestrian traffic monitoring in public spaces.

The work has been partially presented at IEEE Wireless Communication and Networking conference (WCNC 2012), Paris, April 2012.

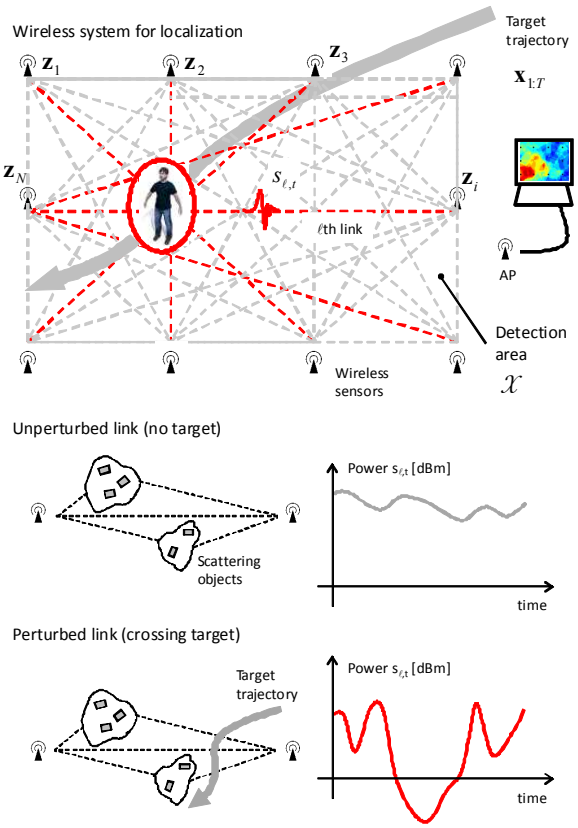

Fig. 1. Wireless infrastructure for device-free localization (top). Received signal power over the ℓth link due to the moving target (bottom figure).

In contrast to well-known mm-wave [3] and ultra-wide band [4] imaging techniques, the device-free localization approach herein considered is capable of using commercial radios operating at 2.4GHz over a small bandwidth (i.e., narrow-band systems) measuring the signal strengths rather than delays of reflections or scattering as for usual monostatic radars. Targets in the radio coverage modify the RSS field in a way that depends on their location relative to the wireless devices so that it is possible to track the target movements from the measured RSS perturbations.

A tomographic method has been proposed in [5] allowing to visually inspect the perturbations of the RSS field and providing an accurate radio imaging of the area of interest. The work highlights a number of open scientific and technical challenges that need to be addressed. These include the definition of a reliable statistical model - and related calibration procedure - to describe the impact of the attenuating/diffracting/scattering target on the RSS measurements and the potential location accuracy that can be drawn from such measurements, in order to support an efficient design of the wireless sensor deployment and the positioning algorithm.

In this paper, the device-free localization problem is cast into a new Bayesian framework based on a stochastic model that allows to describe the target-induced RSS perturbations and optimally exploit all the location information coming from attenuation, random fading and mobility model. A new stochastic model is proposed for relating the RSS measurements over each link to the object position. Since the presence of the target is shown to affect both the attenuation and the random fluctuations of the received power, a log-normal model is defined where the RSS mean and variance are expressed as functions of the target location. The increase of path loss and power fluctuation induced by the moving target are described by exploiting the theory of diffraction: a closed-form analytical model is derived, tailored for the specific localization problem and validated on experimental data. The model is able to describe the variations of the responsiveness of the radio link - herein acting as detector of moving objects - with the target position along the LOS path, highlighting the increased sensitivity close to the transmitting/receiving devices. The model is also used to evaluate fundamental performance limits and to tailor Bayesian tracking algorithms for localization.

The positioning system has been validated by several indoor and outdoor experimental studies. A regular square layout of IEEE 802.15.4 wireless devices has been considered for most of the analysis; nevertheless the RSS model and the positioning method are general enough to be applied to non-regular network topologies and to different classes of wireless networks, such as WiFi or other short-range device-to-device radio technologies deployed in home or public environments. Preliminary results in non-LOS (NLOS) environments with non-regular network deployments are discussed as well. For the implementation of the localization system, the medium access control (MAC) sub-layer protocol has been designed to allow the nodes to cooperatively exchange RSS measurements on a peer-to-peer basis. The protocol enables real-time sampling of the RSS field and provides a practical solution for online target detection and tracking, being fully compatible with the IEEE 802.15.4-2011 standard. For positioning, multi-link measurements are optimally combined in a multi-angulation fashion using two different criteria for estimation: maximum likelihood estimation (MLE) based on snapshot measurements (i.e., without tracking); Bayesian sequential estimation exploiting a-priori information on the target mobility and particle filtering (PF) to alleviate false localization problems [6]. Results from the test-bed measurements confirm that the proposed model provides a reliable description of the RSS changes caused by moving objects and allows to obtain an accurate localization.

II. Problem Formulation

As shown in Fig. 1, the localization system is based on a network of N nodes connected in mesh mode and spread over the region to be monitored $\mathcal{X} \subset \mathbb{R}^2$ (detection area). Devices are acting as anchor nodes being placed at known position $\mathbf{z}_i = [z_{1,i}, z_{2,i}] \in \mathcal{X}$, where $z_{k,i}$ denotes the k-th Cartesian coordinate ($k = 1, 2$) of the i-th node ($i = 1, ..., N$) in the two-dimensional (2D) space. These known positions can be either measured during the deployment phase or estimated by the network itself through a cooperative localization approach [1] [7]. We model the network as an unidirectional connected graph with L active wireless links (edges) indexed as $\ell \in \mathcal{L} = \{1, \ldots, L\}$. The active links experience a sufficiently high signal strength to support reliable communication even in case of obstruction caused by the target. To simplify the reasoning, we assume that the two links associated with the same pair of devices are reciprocal. Experimental tests show that link asymmetry [8] has a marginal influence on our localization modeling and thus justify the assumption.

At discrete time $t = 1, 2, 3, \ldots$, with sampling interval Δt, an access point (AP) acting as sink node collects the set of L noisy measurements $\mathbf{s}_t = [s_{1,t} \cdots s_{L,t}]^T$ where each observation $s_{\ell,t}$ represents the RSS measured on the link $\ell \in \mathcal{L}$ during the t-th time interval. As detailed in Sect. V, the network used for experimental validation employs a proprietary MAC protocol - defined on top of the IEEE 802.15.4 standard - to rule the communication between the N anchor nodes and towards the AP. The N devices perform a periodic and synchronous transmission of probe signals over reserved time-slots, they measure the RSS from the received signals and forward the data to the AP.

A single target[1] is assumed to move within the detection area, with position $\mathbf{x}_t = [x_{1,t}, x_{2,t}] \in \mathcal{X}$ at time t. The target does not need to carry any electronic device and it is not aware of being localized. The problem we tackle is to estimate the position $\mathbf{x}_t$ given the measurements $\mathbf{s}_t$ taken over the L peer-to-peer links up to time t. The position is not directly observable but it is hidden into the noisy RSS measurements $\mathbf{s}_t$ according to the statistical model that will be defined in the following sections.

A. RSS Model for Localization

The signal model here proposed describes how the RSS on each link is related to the target position $\mathbf{x}_t$ in $\mathcal{X}$. The analytical model will be derived with the support of a diffraction-based analysis (Sect. III) and corroborated by experimental results in both indoor and outdoor scenarios (Sect. V).

We assume that the N anchor devices are equipped with a single omnidirectional antenna transceiver. As for typical scenarios, the AP antenna is mounted on an elevated point over

[1] Multi-target analysis is out of the scope of this paper. Extension to multiple targets would require the adaptation of the model so as to describe the effect generated on the received signal power by one, two, etc. targets located along the radio link. Preliminary experiments have been conducted highlighting a certain sensitivity of the system to the presence of multiple targets.

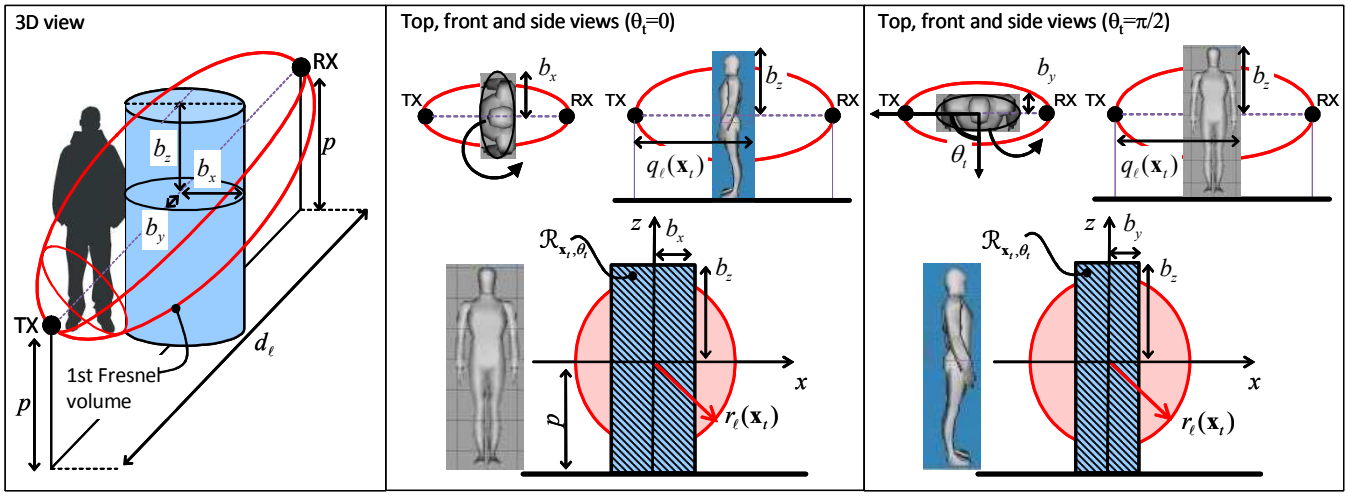

Fig. 2. Diffraction-based model for target object (human body scattering).

flat terrain. Consider a link ℓ as in Fig. 2, a target (a human body in the example) traversing the link induces significant fades on the power $s_{\ell,t}$ [9] and the perturbation depends on the target location relative to the link. Notice that in this work we are interested in the target location regardless of any turn or change of posture that the target may perform in that position; also, the desired accuracy does not need to be higher than the target size. Thereby, the event "target in position $\mathbf{x}_t$" refers to the target being located in the surrounding of $\mathbf{x}_t$ and assuming any orientation (or azimuth) θ_t with respect to the line-of sight (LOS) path, as indicated in Fig. 2. This will give rise to a random fading on the observed RSS due to different orientations or arrangements assumed by the target in $\mathbf{x}_t$.

According to the widely adopted log-normal power model (see e.g., [10]), the RSS $s_{\ell,t}$ expressed in dBm is defined as a Gaussian random variable whose parameters depend on the specific environment. In our model, the probability density function (pdf) parameters are related also to the absence ($\mathbf{x}_t \notin \mathcal{X}$) or presence ($\mathbf{x}_t \in \mathcal{X}$) of the target in the area $\mathcal{X}$:

$$s_{\ell,t} = \begin{cases} h_\ell(\varnothing) + w_\ell(\varnothing), & \text{if } \mathbf{x}_t \notin \mathcal{X} \\ h_\ell(\mathbf{x}_t) + w_\ell(\mathbf{x}_t), & \text{if } \mathbf{x}_t \in \mathcal{X} \end{cases} \tag{1}$$

In case of missing target ($\mathbf{x}_t \notin \mathcal{X}$), the link ℓ experiences an average received power, denoted as $h_\ell(\varnothing)$, that accounts for time-invariant propagation effects such as path-loss and static multipath due to fixed obstructions [11] or scattering objects (metallic reflectors, walls, floor, etc.). On the other hand, the Gaussian noise $w_\ell(\varnothing) \sim \mathcal{N}(0, \sigma^2_\ell(\varnothing))$, with zero mean and standard deviation $\sigma_\ell(\varnothing)$, models the measurement errors due to hardware limits (e.g., quantization, RF processing, etc.) [12] as well as the randomness of shadowing due to variations in the surrounding environment (e.g., objects or people moving outside the detection area $\mathcal{X}$).

In case of target presence ($\mathbf{x}_t \in \mathcal{X}$), the measured RSS is subject to a perturbation that depends on the specific position $\mathbf{x}_t$ within $\mathcal{X}$. As confirmed by our experiments (see also [13]-[15]), considerable perturbations are observed when the target is located within the first Fresnel zone [16] of the link, as this zone typically contributes to 90% of the propagating energy in the wavefield. Both the deterministic path-loss $h_\ell(\mathbf{x}_t)$ and the random fading $w_\ell(\mathbf{x}_t) \sim \mathcal{N}(0, \sigma^2_\ell(\mathbf{x}_t))$ provide information on the target location and are thus modeled as function of $\mathbf{x}_t$. As a matter of fact, a target located along the link typically causes an increased path-loss such that:

$$h_\ell(\mathbf{x}_t) = h_\ell(\varnothing) - \Delta h_\ell(\mathbf{x}_t), \tag{2}$$

where $\Delta h_\ell(\mathbf{x}_t) = h_\ell(\varnothing) - h_\ell(\mathbf{x}_t) \geq 0$ is the additional attenuation due to the obstruction of the LOS path by the target (if the target is outside the sensitivity area of the link $\Delta h_\ell(\mathbf{x}_t) = 0$). In addition, since the target can turn, move or assume different postures in the surrounding of the location $\mathbf{x}_t$, an increased RSS variability is observed:

$$\sigma_\ell(\mathbf{x}_t) = \sigma_\ell(\varnothing) + \Delta\sigma_\ell(\mathbf{x}_t) \tag{3}$$

with $\Delta\sigma_\ell(\mathbf{x}_t) = \sigma_\ell(\mathbf{x}_t) - \sigma_\ell(\varnothing) \geq 0$ denoting the increased standard deviation.

Evaluation of the 2D power maps $\{\Delta h_\ell(\mathbf{x}_t), \Delta\sigma_\ell(\mathbf{x}_t)\}$ is crucial for solving the localization problem. Maps are typically obtained experimentally by raytracing tools [17] or extensive fingerprinting procedures [5]-[18]. In this work, we propose to employ a new and analytically tractable model based on the diffraction theory as described in the next section.

III. Diffraction-based Model for RSS Perturbation

As depicted in the example of Fig. 2, we consider a link ℓ where the distance between the transmitting and receiving anchors is d_ℓ and devices are mounted at the same height $p = 1$m from the ground (flat terrain). The target is modeled as a dielectric elliptic cylinder, with semi-axes of the elliptical cross section denoted as (b_x, b_y), with $b_x \geq b_y$, and height b_z above the LOS path. The target location $\mathbf{x}_t$ is assumed to be along the LOS path, with distance $q_\ell(\mathbf{x}_t) < d_\ell$ from the transmitter[2] and azimuth relative to the LOS path uniformly distributed $\theta_t \sim \mathrm{U}[-\pi, \pi]$. Two examples of configurations with $\theta_t = 0$ and $\theta_t = \pi/2$ are shown in Fig. 2.

[2]The target is located in the far-field region of transmitter and receiver.

We assume that the additional target-induced attenuation $\Delta h_\ell(\mathbf{x}_t)$ and standard deviation $\Delta\sigma_\ell(\mathbf{x}_t)$ characterizing the stochastic model (1) are mainly due to propagating wavefronts diffracting around the target object obstructing the ℓ-th link at position $\mathbf{x}_t$ and with random azimuth θ_t. Furthermore, for any pair $(\mathbf{x}_t, \theta_t)$, the target is acting as a perfectly absorbing knife-edge object. The observed RSS perturbation terms $\Delta h_\ell(\mathbf{x}_t)$ and $\Delta\sigma_\ell(\mathbf{x}_t)$ are computed in Sect. III-A and III-B, as a function of the portion of the Fresnel volume circular cross-section obstructed by the target and thus they depend on the distance $q_\ell(\mathbf{x}_t)$. The diffraction-based model is then validated in Sect. III-C for the relevant case of a human body, in both indoor and outdoor environments, using experimental power maps collected during a calibration phase over relevant set-points $\mathbf{x}_t$. The notation $\cdot|_{\rm dB} = 10\log_{10}(\cdot)$ is used to indicate logarithmic dB conversion.

A. Modeling the Attenuation $\Delta h_\ell(x_t)$

The attenuation $\Delta h_\ell(\mathbf{x}_t)$ averaged over the random object azimuth θ_t, can be modeled as the sum of a term accounting for the diffraction caused by the obstruction and a residual term Δh_0 - evaluated experimentally in Sect. III-C - accounting for additional reflections and refraction effects. It is calculated as:

$$\Delta h_\ell(\mathbf{x}_t) = \underbrace{\mathrm{E}_{\theta_t}\left[\left|\frac{E_0}{E_1(\mathbf{x}_t,\theta_t)}\right|^2\Bigg|_{\rm dB}\right]}_{\text{Diffraction term}} + \Delta h_0, \tag{4}$$

where $\mathrm{E}_\theta\left[f(\theta)\right] = (2\pi)^{-1}\int_{-\pi}^{\pi} f(\theta)d\theta$ denotes the average of the function $f(\theta)$ of the azimuth θ. For target standing at $\mathbf{x}_t$ with any azimuth θ_t, the term $|E_0/E_1(\mathbf{x}_t,\theta_t)|$ represents the electric field loss due to the target obstruction, computed as the ratio between the field received over the obstructed link $E_1(\mathbf{x}_t,\theta_t)$ and the field measured in free space E_0 (i.e., in absence of target). The energy loss due to the diffraction is computed using the Fresnel-Kirchhoff method [19]-[20] here extended to the 2D case taking into account the object profile for varying target orientation. Based on the Huygen's principle, the exponential phase term of the electric field is integrated over the two vertical and lateral dimensions [21] as

$$\left|\frac{E_1(\mathbf{x}_t,\theta_t)}{E_0}\right| = \left|1 - j\int_{(x,z)\in\mathcal{R}_{\mathbf{x}_t,\theta_t}} \frac{\exp\left[-j\pi\frac{x^2+z^2}{r_\ell^2(\mathbf{x}_t)}\right]}{r_\ell^2(\mathbf{x}_t)}dxdz\right|, \tag{5}$$

where (x, z) denote the axes of the 2D plane orthogonal to the LOS path at location $\mathbf{x}_t$. The region $\mathcal{R}_{\mathbf{x}_t,\theta_t}$ indicates the area occupied by the target object in this plane, as illustrated in Fig. 2 for the relevant cases $\theta_t = 0$ and $\theta_t = \pi/2$. The term $r_\ell(\mathbf{x}_t)$ is the radius of the circular cross-section of the first Fresnel volume, measured at the location $\mathbf{x}_t$ along the link[3]:

$$r_\ell(\mathbf{x}_t) = \sqrt{\lambda\frac{q_\ell(\mathbf{x}_t)\left[d_\ell - q_\ell(\mathbf{x}_t)\right]}{d_\ell}}, \tag{6}$$

[3]The approximation uses the distances measured along the ground rather than along the direct wave.

with λ denoting the signal wavelength. The maximum radius $r_\ell(\mathbf{x}_t) = 1/2\sqrt{\lambda d_\ell}$ is observed for $q_\ell(\mathbf{x}_t) = d_\ell/2$. Exact solutions to the integral (5) can be found in [21].

Assuming that the vertical dimension of the object is larger than the Fresnel circular section, $b_z > r_\ell(\mathbf{x}_t)$, and that $b_z \gg b_x$, the attenuation (4) can be approximated as

$$\Delta h_\ell(\mathbf{x}_t) \simeq \gamma_1\left(\frac{b_x^2 + b_y^2}{r_\ell^2(\mathbf{x}_t)}\right)\Bigg|_{\rm dB} + \Delta h_0, \tag{7}$$

with $\gamma_1 = \pi^2/2$ (see proof in the Appendix). The approximation will be validated experimentally in Sect. III-C. From (7) we can conclude that the increase of attenuation is ruled by the fraction of the Fresnel cross-section obstructed by the target. Being the vertical target size $b_z > r_\ell(\mathbf{x}_t)$, the only relevant factor for attenuation is the lateral obstruction represented by the ratios $b_x/r_\ell(\mathbf{x}_t)$ and $b_y/r_\ell(\mathbf{x}_t)$ between the width of the obstruction cross-section $\mathcal{R}_{\mathbf{x}_t,\theta_t}$ and the Fresnel radius $r_\ell(\mathbf{x}_t)$ in the two extreme cases $\theta_t = 0$ and $\theta_t = \pi/2$. The term $(b_x^2 + b_y^2)/r_\ell^2(\mathbf{x}_t)$ approximates the average square obstruction for the rotating target.

B. Modeling the Standard Deviation $\Delta\sigma_\ell(\mathbf{x}_t)$

The increase of standard deviation is due to the random azimuth θ_t and it is calculated as

$$\Delta\sigma_\ell(\mathbf{x}_t) = \mathrm{std}_{\theta_t}\left[\left|\frac{E_0}{E_1(\mathbf{x}_t,\theta_t)}\right|^2\Bigg|_{\rm dB}\right] + \Delta\sigma_0, \tag{8}$$

with $\mathrm{std}_{\theta_t}\left[f(\theta)\right] = \sqrt{(2\pi)^{-1}\int_{-\pi}^{\pi}\left(f(\theta) - \mathrm{E}_{\theta_t}\left[f(\theta)\right]\right)^2 d\theta}$ and loss term $E_1(\mathbf{x}_t,\theta_t)/E_0$ defined as in (5). The residual term $\Delta\sigma_0$ - evaluated experimentally in Sect. III-C - models the contribution of further reflections and refraction effects caused by the target and not accounted for in the diffraction analysis. Similarly as for the signal attenuation, the simplified model used for localization assumes that $b_z \gg b_x$ and $b_x \geq b_y$, which leads to the result:

$$\Delta\sigma_\ell(\mathbf{x}_t) \simeq \gamma_1\left(\frac{b_x^2 - b_y^2}{r_\ell^2(\mathbf{x}_t)}\right)\Bigg|_{\rm dB} + \Delta\sigma_0, \tag{9}$$

(see the Appendix for the proof). As confirmed by the experimental radio measurements outlined in Sect. III-C, the random orientation of the object located at position $\mathbf{x}_t$ within the link area causes the standard deviation term to increase for any practical case such that $b_x \neq b_y$. Unbalanced geometric dimensions of the target (e.g., for $b_x \gg b_y$) cause significant variations of the obstruction area with the random azimuth θ_t and consequently an increase of the RSS fluctuations around the average term $\Delta h_\ell(\mathbf{x}_t)$.

C. Single-link Model Calibration

The proposed models (7) and (9) have been validated through indoor and outdoor measurement campaigns. The parameters characterizing the diffraction model have been obtained by post-processing of the measurements. The following tests consider a single link where two IEEE 802.15.4 devices are deployed at distance $d_\ell = 4$m and $d_\ell = 8$m,

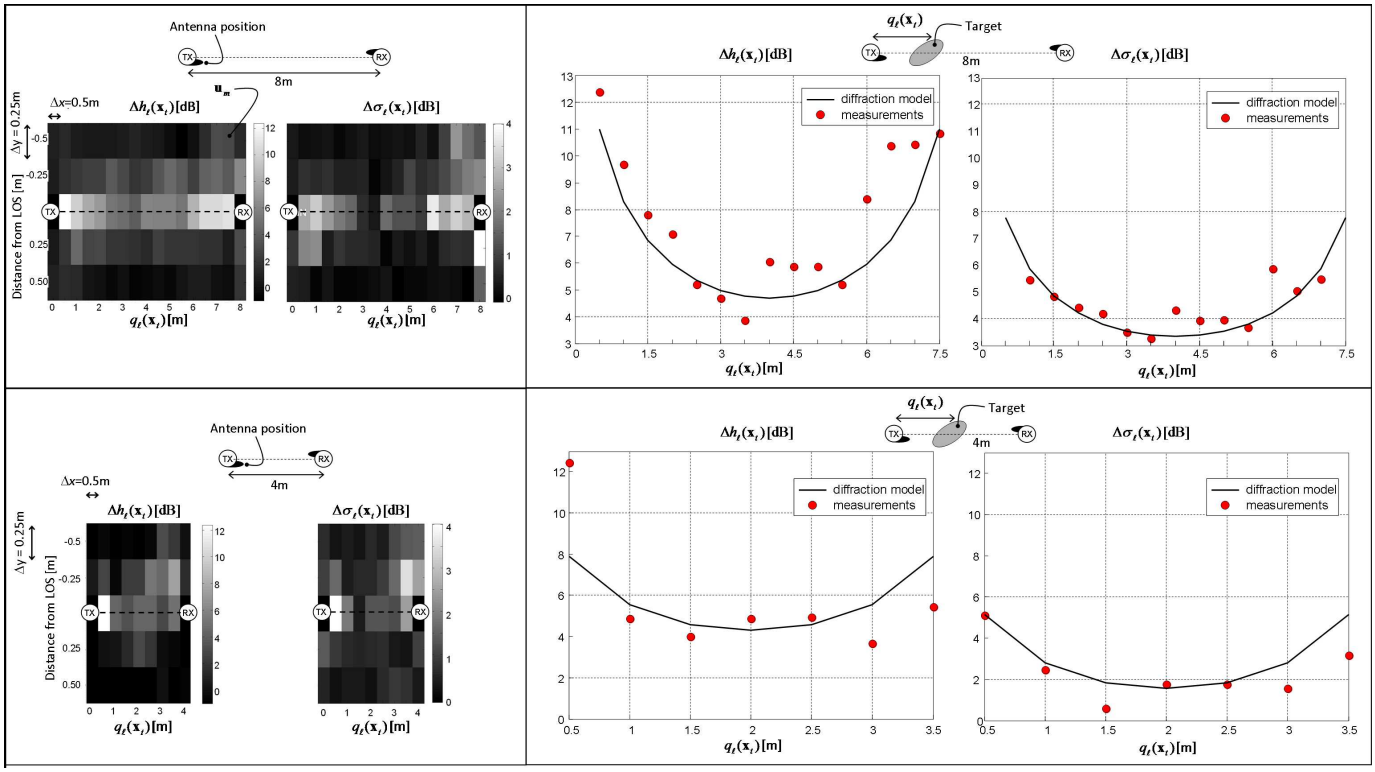

Fig. 3. Indoor tests for single-link sensitivity region: measurements and diffraction-based model calibration

respectively. As depicted in Fig. 3 for the indoor scenario, a human body target moves along a known trajectory that covers M positions $\{\mathbf{u}_m\}_{m=1}^{M} \in \mathcal{X}$ over a regular grid. The grid is characterized by intervals of $\Delta x = 50$cm along the LOS path and $\Delta y = 25$cm along the direction orthogonal to the LOS path. The target stays in each position $\mathbf{u}_m$ for a period of 10s, turning and moving within the spatial bin, randomly changing its orientation θ_t and thus the size of the obstruction area $\mathcal{R}_{\mathbf{x}_t,\theta_t}$. The corresponding RSS samples associated with the binned position $\mathbf{u}_m$ and collected by the receiver during the 10s period are used to evaluate a sample average $h_\ell(\mathbf{u}_m)$ and a sample standard deviation $\sigma_\ell(\mathbf{u}_m)$. Each pixel of the four gray scale maps in Fig. 3 represents the measured average path-loss $\Delta h_\ell(\mathbf{u}_m)$ and standard deviation $\Delta\sigma_\ell(\mathbf{u}_m)$ increase (in dB) compared to the case of no target. The examples consider two indoor links with distance $d_\ell = 8$m (top) and $d_\ell = 4$m (bottom), respectively. The diffraction effect can be mostly appreciated along the LOS path, minor (but still significant) effects can be observed within the first Fresnel volume.

For the attenuation, the *sensitivity region* $\mathcal{X}_\ell^{(a)} \subset \mathcal{X}$, defined as the locus of positions where the target generates a significant path-loss increase Δh_ℓ (ranging from 4dB to 12dB), is shaped as a strip of width 5-6λ centered around the direct path connecting the two nodes, $\lambda = 0.125$m being the carrier wavelength. A similar reasoning holds for the standard deviation: for any link ℓ, the sensitivity region $\mathcal{X}_\ell^{(s)} \subset \mathcal{X}$ now defines the locus of positions where a significant change in the standard deviation could be observed due to the target presence. Compared to the attenuation, the strip region for the standard deviation is characterized by a larger width, approximately 6-7λ, therefore $\mathcal{X}_\ell^{(a)} \subseteq \mathcal{X}_\ell^{(s)}$: this is also confirmed by the experiments illustrated in Sect. 5. The standard deviation increase $\Delta\sigma_\ell$ is 1dB÷5dB.

The four plots on the right side of Fig. 3 are instrumental to the validation of the diffraction model (7) for the attenuation and (9) for the standard deviation. The plots show the increase of average attenuation $\Delta h_\ell(\mathbf{u}_m)$ and standard deviation $\Delta\sigma_\ell(\mathbf{u}_m)$ for $\mathbf{u}_m$ belonging to the LOS path, i.e., the sections along the LOS path of the 2D power maps on the left figures. For each case, the diffraction model is superimposed in solid lines. The object has size $b_x \simeq 20$cm and $b_y \simeq 14$cm while the target volume within the (x,y) plane is confined within an area of $4b_xb_y \simeq 0.12\text{m}^2$. Observed residual terms due to reflections and refractions are $\Delta h_0 = 1.5$dB and $\Delta\sigma_0 = 3.5$dB, for $d_\ell = 4$m, $\Delta h_0 = 3.5$dB and $\Delta\sigma_0 = 4.5$dB for $d_\ell = 8$m. The reflection/refraction components are shown to have a more significant impact for larger distance as $d_\ell = 8$m. As predicted by the model, the amount of path loss increase caused by the target depends on the position of the obstructing object along the LOS path and thus on the distance $q_\ell(\mathbf{x}_t)$ from the transmitter. The behavior can be better appreciated for large distances, i.e., $d_\ell = 8$m, rather than smaller distances, i.e., $d_\ell = 4$m, as the fraction of obstructed Fresnel cross-section is larger in the first case. The impact is more significant on the path-loss increase rather than on the standard deviation. Based on further experiments here not included, we observed that the accuracy of the RSS model is higher in outdoor compared to indoor. This is due to reflections from surrounding walls and furniture not considered by the diffraction model.

When the target position is outside the LOS path (but still

inside the corresponding strip regions $\mathcal{X}_\ell^{(a)}$, $\mathcal{X}_\ell^{(s)}$) the observed link sensitivity is reduced as predicted by the diffraction integral in (5): for the test-bed (see Sect. V) a Gaussian decaying function is adopted to approximate the attenuation and standard deviation behavior within the strip (along the direction perpendicular to the LOS path).

IV. Positioning Algorithms and Performance

For on-line tracking[4] of the target location $\mathbf{x}_t$ from the observed data $\mathbf{s}_{1:t} = [\mathbf{s}_1 \cdots \mathbf{s}_t]$, we employ Bayesian sequential estimation. The target motion is modeled as a first-order Hidden Markov Model (HMM), $\mathbf{x}_t = \mathbf{x}_{t-1} + \mathbf{v}_t$, where $\mathbf{v}_t$ denotes the driving process with known distribution $f_{\mathbf{v}_t}(\mathbf{v})$[5]. Transition probabilities are given by $p(\mathbf{x}_t|\mathbf{x}_{t-1}) = f_{\mathbf{v}_t}(\mathbf{x}_t - \mathbf{x}_{t-1})$. The initial state distribution $p(\mathbf{x}_1)$, for any $\mathbf{x}_1 \in \mathcal{X}$, is chosen based on the available a-priori information about the target object position at time $t = 1$: it can be uniform over the whole monitored area or over the related boundary, shaped according to the access areas of the considered environment, or impulsive in case of knowledge of the starting position.

The state $\mathbf{x}_t$ is hidden into the observation $\mathbf{s}_t$, whose L components are assumed to be conditionally independent given the location $\mathbf{x}_t$. Recalling the model (1), the measurement $\mathbf{s}_t$ conditioned to $\mathbf{x}_t$ is an uncorrelated Gaussian vector with mean $\mathbf{h}(\mathbf{x}_t) = [h_1(\mathbf{x}_t) \cdots h_L(\mathbf{x}_t)]^T$ and covariance $\mathbf{C}(\mathbf{x}_t) = \mathrm{diag}\left(\sigma_1^2(\mathbf{x}_t), \ldots, \sigma_L^2(\mathbf{x}_t)\right)$. The conditioned pdf follows as:

$$p(\mathbf{s}_t|\mathbf{x}_t) = \frac{1}{(2\pi)^{L/2}|\mathbf{C}(\mathbf{x}_t)|^{1/2}} \exp\left\{-\frac{1}{2}\left\|\mathbf{s}_t - \mathbf{h}(\mathbf{x}_t)\right\|^2_{\mathbf{C}^{-1}(\mathbf{x}_t)}\right\} \tag{10}$$

where $\|\mathbf{s}\|^2_{\mathbf{C}} = \mathbf{s}^{\mathrm{T}}\mathbf{C}\,\mathbf{s}$ denotes the square norm of the vector $\mathbf{s}$ weighted by the matrix $\mathbf{C}$. A snapshot MLE of $\mathbf{x}_t$ can be obtained by maximizing the likelihood of the measurement $\mathbf{s}_t$ at time t as $\hat{\mathbf{x}}_t = \arg\max_{\mathbf{x}_t \in \mathcal{X}} p(\mathbf{s}_t|\mathbf{x}_t)$. On the other hand, the Bayesian approach allows us to exploit the a-priori information on the target motion and to recursively derive the a-posteriori pdf as [24]:

$$p(\mathbf{x}_t|\mathbf{s}_{1:t}) \propto p(\mathbf{s}_t|\mathbf{x}_t) \underbrace{\int_{\mathcal{X}} p(\mathbf{x}_t|\mathbf{x}_{t-1}) p(\mathbf{x}_{t-1}|\mathbf{s}_{1:t-1}) d\mathbf{x}_{t-1}}_{p(\mathbf{x}_t|\mathbf{s}_{1:t-1})}, \tag{11}$$

where unimportant constant terms have been neglected. The a-priori pdf $p(\mathbf{x}_t|\mathbf{s}_{1:t-1})$ is obtained from the a-posteriori pdf of the previous step $p(\mathbf{x}_{t-1}|\mathbf{s}_{1:t-1})$ and the knowledge of the transition probabilities $p(\mathbf{x}_t|\mathbf{x}_{t-1})$ for any $t > 1$. It is initialized with $p(\mathbf{x}_t|\mathbf{s}_{1:t-1}) = p(\mathbf{x}_1)$ for $t = 1$. Once the a-posteriori pdf is calculated using (11), the estimate of the state $\mathbf{x}_t$ is obtained using either the maximum-a-posteriori (MAP) $\hat{\mathbf{x}}_t = \arg\max_{\mathbf{x}_t \in \mathcal{X}} p(\mathbf{x}_t|\mathbf{s}_{1:t})$ or the minimum mean square error (MMSE) criterion $\hat{\mathbf{x}}_t = \int_{\mathcal{X}} \mathbf{x}_t p(\mathbf{x}_t|\mathbf{s}_{1:t}) d\mathbf{x}_t$.

For the evaluation of the a-posteriori pdf (11) we consider a grid sampling of the location space $\mathcal{X}$ (grid-based filtering or GF [22]) and a sequential importance sampling (particle filtering or PF [6]). The GF approach is based on a regular 2D grid of K spatial positions, with spatial sampling interval Δx over the two dimensions; the pdfs are evaluated over the K grid points and the integral in (11) is approximated by a finite sum [25]. The more efficient PF approach relies on random sampling with K particles (and associated weights) optimally selected at each time step according to the importance sampling principle [24].

A. Performance Metrics and Bounds

The Cramer Rao Bound (CRB) is a useful performance benchmark for assessing the localization algorithms or optimizing the anchors' deployment. Here we are specifically interested in the maximum accuracy that can be obtained from the RSS measurements exploiting the analytical maps (7) and (9) for all the active links; we do not consider in this analysis any a-priori knowledge drawn from the target dynamics model or other a-priori information on the target position[6].The aim is to explore the potentiality of the cooperative passive monitoring system.

The CRB provides a lower bound on the covariance matrix for any unbiased estimator $\hat{\mathbf{x}}$ of the target position $\mathbf{x} = [x_1, x_2]^T$ [26]:

$$\mathrm{Cov}\left(\hat{\mathbf{x}}\right) = \mathrm{E}[(\hat{\mathbf{x}} - \mathbf{x})(\hat{\mathbf{x}} - \mathbf{x})^{\mathrm{T}}] \geq \mathbf{CRB}\left(\mathbf{x}\right) = \mathbf{F}^{-1}\left(\mathbf{x}\right), \tag{12}$$

where $\mathbf{F}\left(\mathbf{x}\right)$ is the 2×2 Fisher information matrix (FIM). According to the model (1), the FIM elements $F_{i,j} = [\mathbf{F}\left(\mathbf{x}\right)]_{i,j}$, for $i, j \in \{1, 2\}$, can be evaluated from the 2D maps of power loss $h_\ell\left(\mathbf{x}\right)$ and standard deviation $\sigma_\ell\left(\mathbf{x}\right)$ as

$$F_{1,1} = \sum_{\ell=1}^{L} \frac{1}{\sigma_\ell^2(\mathbf{x})} \left[\left(\frac{\partial h_\ell\left(\mathbf{x}\right)}{\partial x_1}\right)^2 + 2\left(\frac{\partial \sigma_\ell\left(\mathbf{x}\right)}{\partial x_1}\right)^2\right] \tag{13}$$

$$F_{2,2} = \sum_{\ell=1}^{L} \frac{1}{\sigma_\ell^2(\mathbf{x})} \left[\left(\frac{\partial h_\ell\left(\mathbf{x}\right)}{\partial x_2}\right)^2 + 2\left(\frac{\partial \sigma_\ell\left(\mathbf{x}\right)}{\partial x_2}\right)^2\right] \tag{14}$$

for the main diagonal entries and

$$F_{1,2} = \sum_{\ell=1}^{L} \frac{1}{\sigma_\ell^2(\mathbf{x})} \left[\frac{\partial h_\ell\left(\mathbf{x}\right)}{\partial x_1}\frac{\partial h_\ell\left(\mathbf{x}\right)}{\partial x_2} + 2\frac{\partial \sigma_\ell\left(\mathbf{x}\right)}{\partial x_1}\frac{\partial \sigma_\ell\left(\mathbf{x}\right)}{\partial x_2}\right] \tag{15}$$

for the off-diagonal ones. The gradient functions $\frac{\partial h_\ell(\mathbf{x})}{\partial x_i}$ and $\frac{\partial \sigma_\ell(\mathbf{x})}{\partial x_i}$, for $i \in \{1, 2\}$, embody the information on the target location provided by the RSS attenuation $h_\ell(\mathbf{x})$ and standard deviation $\sigma_\ell(\mathbf{x})$ maps, respectively. A performance metric of practical relevance is the lower bound on the mean square error (MSE) of the position estimate:

$$\mathrm{MSE} = \mathrm{E}[|\hat{\mathbf{x}} - \mathbf{x}|^2] \geq \mathrm{tr}[\mathbf{F}^{-1}\left(\mathbf{x}\right)]. \tag{16}$$

which will be evaluated in the subsequent analysis.

[4]Extension to joint detection-tracking can be obtained by modifying the Markovian motion model to include an additional state that denotes the target absence and defining the transition probabilities to/from such state (target unlock/lock) as in [22].

[5]Extension of the HMM to account for target velocity can be obtained by employing e.g., a random force model [23].

[6]Extension to the Bayesian CRB for location tracking can be derived based on the work in [23]

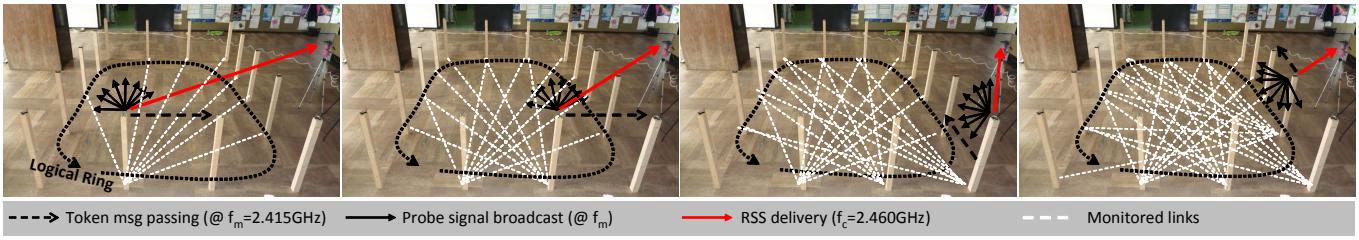

Fig. 4. Network architecture for device-free localization: timed-token beacon message passing.

V. Experimental Activities

In the proposed experimental setup, the device-free localization system is implemented over battery-powered transceivers based on the low-power single-chip 2.4 GHz IEEE 802.15.4 compliant device CC2420 [27]. The processor board is equipped with the ATmega128L microcontroller. Experiments have been carried out in indoor and outdoor sites: the first site is an open-space room; the second site is an open outdoor area characterized by flat terrain. In both tests, $N = 14$ nodes are regularly deployed along the boundary of a $5\text{m}\times 4\text{m}$ area, according to the geometry in Fig. 4 (for indoor). The target is a person moving inside the area. Radio transmit power is set to 0dBm. For all cases we considered omnidirectional, vertically polarized antennas, with 2dBi gain: antennas with such a gain can be commonly found on the market and do not require special alignments. An 8-bit RSS indicator (RSSI) is used to measure the RSS, here ranging between -90dBm and -30dBm. The processor board of the AP node collecting data from the sensors is equipped with a Texas Instruments MSP430 microcontroller. Measurements are sent to a PC for data processing and imaging according to the MAC protocol that is discussed in Sect. V-A.

The proposed localization method is validated by means of the following two steps:

1. Trajectory-based multi-link calibration. A person, with similar characteristics of the intended target, moves according to a known training trajectory that spans M different positions $\{\mathbf{u}_m\}_{m=1}^{M} \in \mathcal{X}$. The AP collects and synchronizes the RSS observations received from the sensors. A sample average $h_\ell(\mathbf{u}_m)$ and a sample standard deviation $\sigma_\ell(\mathbf{u}_m)$ is calculated from the collected measurements for each link. These samples are then used to calibrate and validate the parametric model functions $\Delta h_\ell(\mathbf{x}_t)$ and $\Delta\sigma_\ell(\mathbf{x}_t)$, in (7) and (9) respectively[7]. Since only few parameters need to be trained (not necessarily over all links), the parameters can be updated periodically, even during on-line tracking phase, by expectation-maximization (or Baum-Welch) training procedures [25]. This overcomes the limit of non-parametric fingerprinting methods that rely on an extensive and time-consuming calibration; they are highly sensitive to possible changes in the environment and thus only suited for small quasi-static environments. The comparison between the 2D analytical maps and experimental maps obtained by fingerprinting procedures is carried out in Sect. V-B.

2. Target localization and tracking. At each time instant t, each sensor measures and forwards to the AP the RSS samples observed over its active links. The data set $\mathbf{s}_t$ collected by the AP is then used for the estimation of the object position $\hat{\mathbf{x}}_t$ based on the knowledge of the 2D analytical maps. Compared to tomographic imaging solutions, the adoption of the diffraction-based Bayesian methodology provides a clear advantage in terms of complexity and workload of the on-line estimation. The use of the parametric RSS model avoids time-consuming link-by-link calibration, the system can be therefore implemented with minimal low-level software adaptation and integrated with RSS-based active localization systems (see e.g. [23], using the same network for passive and active localization). In contrast, tomographic methods appear to be less promising in terms of flexibility and scalability.

Focusing on the square network layout chosen here as case study, the fundamental performance limits are analyzed in Sect. V-C based on the CRB (as defined in Sect. IV). These limits are then compared to the localization performance obtained from the experimental data by snapshot MLE and Bayesian tracking in Sect. V-D. Finally, preliminary results for device-free localization in more complex mixed LOS/NLOS environments are illustrated in Sect. V.E to support ambient-intelligence services.

A. Network Protocols for Localization

The radio imaging system has stricter reliability and delay requirements compared to conventional WSN applications. The real-time constraint prescribes that the whole observation data set $\mathbf{s}_t$ should be decoded and processed by the AP before a new data set $\mathbf{s}_{t+1}$ is generated after Δt sec. This hard deadline defines a lower-bound on the interval among two consecutive localization updates. In addition, the RSS sampling time interval Δt needs to be adapted to the target mobility model. Assuming that the target velocity is below 1m/s, here the sampling interval is set to $\Delta t = 120$ms.

The proposed MAC sub-layer uses a timed-token message passing protocol [28] on top of the IEEE 802.15.4 compliant network illustrated in Fig. 4. Medium access is based on time division while token message exchange (dashed black arrows) is used to periodically synchronize the network: the slotted Carrier Sense Multiple Access with Collision Avoidance (CSMA-CA) implemented by the IEEE 802.15.4 compliant devices is modified so that the back-off function is

[7]To improve the estimation of model parameters, the training trajectories are repeated (3 times in our experiments). Our experiments show that the attenuation and standard deviation terms characterizing the RSS perturbations for each target position can be reasonably considered as static.

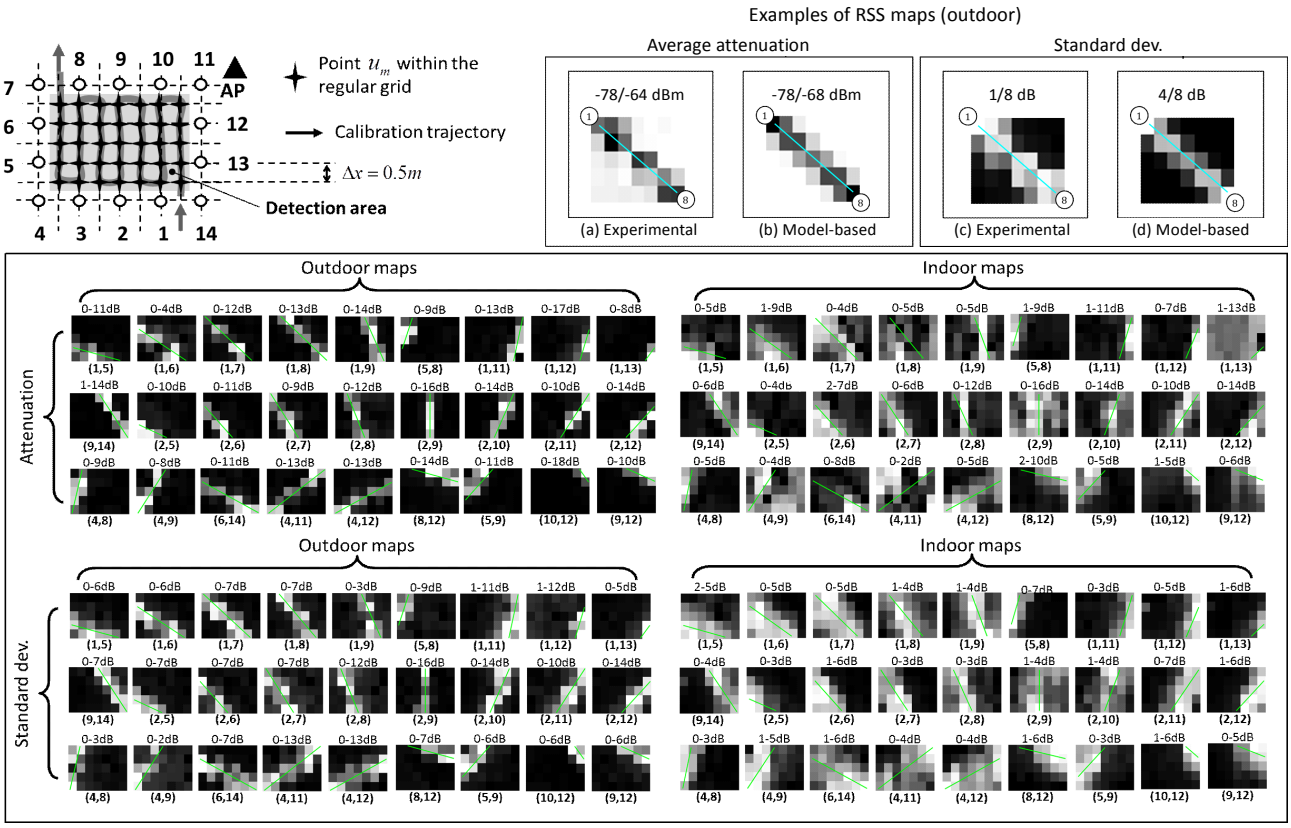

Fig. 5. Top-left corner sub-figure: network layout for the indoor tests. Top-right corner sub-figure: example of experimental maps for the average attenuation (a) and standard deviation (c) for link (1,8) and corresponding diffraction-based analytical maps with the same resolution in subfigures (b) and (d). Bottom sub-figures: experimental average attenuation and standard deviation maps (differential maps) for selected links.

disabled. An energy scan to detect cross-tier interference - by clear channel access (CCA) - is performed at the beginning of the assigned slot; in case the channel is sensed as free the transmission of the token frame is performed with the acknowledgement option disabled. The error control system is based on implicit acknolwedgements. Each device is configured to wait for the token message: in case of a packet drop, a real-time error controller guarantees the generation of a new token after the time-to-token-visit listening time expires. The token frame structure is based on the IEEE 802.15.4 beacon frame type: when the device receives the token message it is configured to perform two tasks: *i)* transmit the backlog of RSS measurements embedded into a IEEE 802.15.4 data frame over a default channel used for communication with the AP (red arrows); *ii)* broadcast the beacon probe signal (solid arrow) over a pre-configured channel.

B. Multi-link Model Calibration: Outdoor/Indoor Scenarios

During the calibration phase, a person moves along a known training trajectory of $M = 35$ positions $\{\mathbf{u}_m\}_{m=1}^{M}$ as indicated in Fig. 5 (top left corner) with a velocity of approximately 1m/s, yielding 8 RSS samples per position on average. The choice for 8 RSS samples is reasonable as far as *i)* the person is moving with velocity around 1m/s; *ii)* the (noisy) information about the attenuation and standard deviation are combined with a-priori information about the target mobility. The trajectory covers all the $K = 7 \times 5$ locations of the 2D regular grid used for approximating the state space $\mathcal{X}$, with spatial sampling interval $\Delta x = 0.5$m. For illustrative purpose, a detailed view of the outdoor attenuation and standard deviation maps, $h_\ell(\mathbf{x}_t)$ and $\sigma_\ell(\mathbf{x}_t)$ respectively, for the link $(1, 8)$ between nodes 1 and 8, is reported in the top-right corner of Fig. 5 (sub-figures (a) and (c)). For the considered link, the average RSS ranges between -78dBm and-64dBm while the standard deviation is in the range of 1-8dB. Corresponding maps in sub-figures (b) and (d) are obtained analytically based on the diffraction model in Sect. III. The colormap has been normalized for each map to the range of values indicated on top of the sub-figure. The resulting maps highlight the accuracy of the diffraction model in predicting the RSS fluctuations within the strip-sized sensitivity areas. The average attenuation, $\Delta h_\ell(\mathbf{u}_m)$, and the standard deviation increase, $\Delta\sigma_\ell(\mathbf{u}_m)$, along the positions of the target obstructing the LOS path are obtained from (7) and (9), respectively. A Gaussian decaying profile is used to model the reduced attenuation and standard deviation outside the LOS path (but inside the corresponding strip regions $\mathcal{X}_\ell^{(a)}$, $\mathcal{X}_\ell^{(s)}$).

Sub-figures at bottom of Fig. 5 represent the differential 2D maps for the attenuation, $\Delta h_\ell(\mathbf{x}_t)$, and standard deviation, $\Delta\sigma_\ell(\mathbf{x}_t)$, calculated from the RSS measurements gathered along the training trajectory. The 2D maps are shown for a selected subset of links $\ell = (i, j)$, with nodes $i = 1, ..., N$ and $j = 1, ..., N$ numbered as in the top-left corner sub-

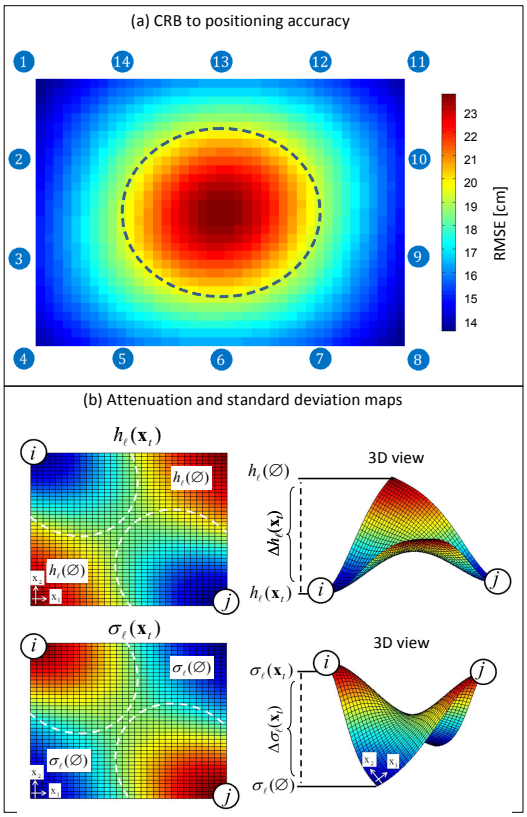

Fig. 6. (a) CRB on the location estimate accuracy (expressed in cm) for the square network deployment; (b) Attenuation and standard deviation analytical maps for the single link (i, j) based on the diffraction model.

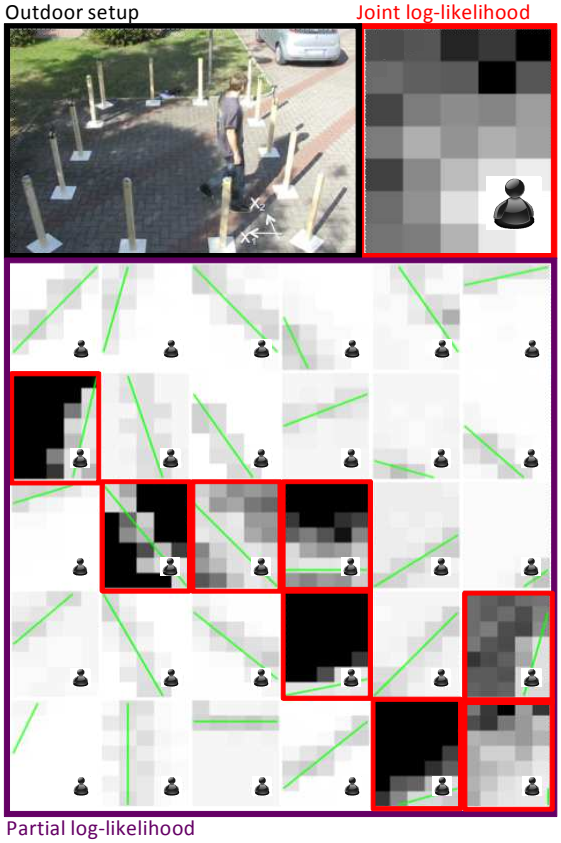

Fig. 7. Joint and partial log-likelihood functions for selected links and for target located in the top right corner of the rectangular layout.

figure. Similarly as in Fig. 3, the maps provide a statistical description of the change in attenuation and standard deviation caused by the moving target. The strip-shaped region defining the sensitivity for link ℓ is now centered around the direct path (highlighted in green color) connecting the corresponding anchor nodes.

In the indoor tests the observed strip widths for attenuation and standard deviation are larger compared to those observed in the corresponding outdoor tests. For the outdoor tests the observed attenuation strip region $\mathcal{X}_\ell^{(a)}$ has width of about 4-5λ, while the strip region $\mathcal{X}_\ell^{(s)}$ for the standard deviation has a larger size of 5-6λ. The observed strip width for the outdoor scenario reasonably fits with the maximum size (or diameter) of the first Fresnel volume cross-section (6), $\sqrt{\lambda d_\ell} \simeq 5.65\lambda$ with $d_\ell \simeq 4$m for the considered case study. The observed strip size for the indoor tests is larger and reasonably matches with the one observed in the single-link tests (Sect. III-C). The results obtained in the indoor scenario can be attributed to the higher amount of reflections and multipath compared to the outdoor open area. This typically leads to a lower accuracy of localization in indoor scenarios compared to outdoor, motivating the use of Bayesian tracking to reduce the location errors.

By looking at the 2D maps in Fig. 5, it is reasonable to conclude that only the *joint* exploitation of the attenuation and the standard deviation maps, possibly combined with prior information from motion modeling, can provide enough information for accurate mobile positioning. The optimal combination of attenuation and fluctuation information for all links into the location belief allows to turn the measurement uncertainty (i.e., the noise $w_\ell(\mathbf{x}_t)$) into an advantage.

The strip-shaped sensitivity regions highlighted by the same maps suggest to define a decision-directed approach for model adjustment during the on-line localization. An automatic procedure can jointly and periodically update the link-dependent propagation parameters $\{h_\ell(\varnothing), \sigma_\ell(\varnothing)\}$ observed in absence of the target and the diffraction parameters $\{\Delta h_0, \Delta\sigma_0\}$ for the target moving within the strip region. Any new observation $\mathbf{s}_t$ indicating a target at position $\hat{\mathbf{x}}_t \in \mathcal{X}_\ell^{(a)}$ (or $\hat{\mathbf{x}}_t \in \mathcal{X}_\ell^{(s)}$ for standard deviation) can be used to update on-line the diffraction model parameters $\{\Delta h_0, \Delta\sigma_0\}$ along the link ℓ sensitivity region and the propagation parameters $\{h_\ell(\varnothing), \sigma_\ell(\varnothing)\}$ for the remaining links not affected by the presence of the target.

C. CRB Analysis

The analysis of the CRB presented in this section provides a theoretical framework for the evaluation of fundamental limits to the positioning accuracy that can be reached by jointly exploiting the analytical maps for RSS attenuation and standard deviation, in (7) and (9) respectively. In Fig. 6-(a) the theoretical root MSE (RMSE) bound to the localization accuracy is analyzed for different positions of the target within the detection area. Positions over a regular grid spanning the

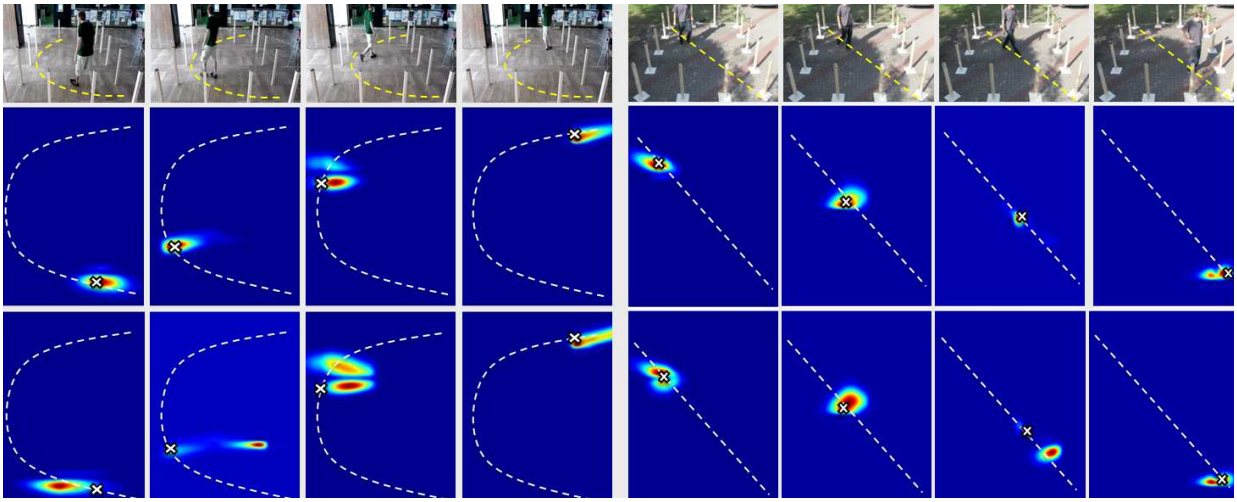

Fig. 8. Top: indoor test environment with human target moving along a trajectory obtained from the experiments. Bottom: location belief images obtained by snapshot MLE and Bayesian tracking, as likelihood function and a-posteriori pdf respectively, for positions corresponding to the top sub-figures.

whole detection area are considered, as the geometric factor (i.e., the impact on the localization accuracy of the nodes' deployment relative to the target location) and the different sensitivity of the RSS measurements along the link, make the localization accuracy space-varying. The corresponding diffraction-based analytical maps for the attenuation $h_\ell(\mathbf{x}_t)$ and standard deviation $\sigma_\ell(\mathbf{x}_t)$ used to compute the FIM $\mathbf{F}(\mathbf{x})$ in (12) are illustrated in Fig. 6-(b) where the Gaussian decaying function approximates the decaying profile of the sensitivities along the direction perpendicular to the LOS path. As outlined in Sect. III, the diffraction effect predicts a higher sensing capability of the radio link (in terms of both attenuation and standard deviation) for targets close to the transmitter/receiver anchors, compared to the sensitivity that would be observed for targets located in-between the two nodes. As highlighted in Fig. 6-(a), the localization error is maximum when the target is confined in the area (highlighted in dashed lines) in the center of the deployment, with RMSE= 21-24cm. Notice that this is the area where most of links are intercepted (i.e., where a good geometric factor would be expected), but the effect of the reduced sensitivity of each link (which depends on the link length) prevails over the multiplicity of the sensing links in this case. In the following section, we will show that this conclusion is confirmed also by experimental results on the localization performance.

D. Mobile Positioning Performance

In Fig. 7-8 we analyze the performance of the MLE and Bayesian MMSE localization methods, that have been implemented using the diffraction-based RSS model calibrated as discussed in Sect. V-B. The regular grid-based sampling considered for the evaluation of the location beliefs, with $M = 35$ grid positions, is also described in Sect. V-B.

Fig. 7 shows the partial log-likelihood maps $\log p(s_{\ell,t}|\mathbf{x}_t)$ for 30 selected links as a function of the M grid positions. The corresponding joint log-likelihood map $\log p(\mathbf{s}_t|\mathbf{x}_t) = \sum_{\ell=1}^{L} \log p(s_{\ell,t}|\mathbf{x}_t)$ is illustrated in the top-right corner sub-figure. The target is located at position $\mathbf{x}_t$ as indicated in the top-left corner sub-figure. The partial log-likelihood maps confirm the effectiveness of the stochastic model illustrated in Sect. III. The subset of links highlighted in red corresponds to the most informative cases where the target is located inside the link sensitivity strips (i.e., inside the areas around the LOS paths connecting transmitter and receiver). For those links the likelihood function takes substantially larger values inside the strip compared to the values observed outside the same strip. For the remaining links instead, being the target located outside the corresponding sensitivity region, the likelihood function inside the strip takes lower values compared to those observed in the outer area.

In Fig. 8 we compare the location belief images provided by snapshot MLE and GF Bayesian estimation, given that the human target is standing in four different positions indicated by markers inside the detection area for both indoor and outdoor scenarios. The transition probabilities $p(\mathbf{x}_t|\mathbf{x}_{t-1})$ for Bayesian tracking are based on a random walk model with 2D uniform pdf $f_{\mathbf{v}_t}(v)$ and standard deviation $\sigma_v = 0.58$m (along each dimension), corresponding to $\sigma_v/\Delta t = 4.8$m/s. The starting distribution $p(\mathbf{x}_1)$ is uniform over the whole detection area. Considering the spatial node density and the number of samples (grid points) used for tracking, initialization is not a critical issue in the considered scenario[8]. Belief images now represent the likelihood function $p(\mathbf{s}_t|\mathbf{x}_t)$ for MLE and the a-posteriori pdf $p(\mathbf{x}_t|\mathbf{s}_{1:t})$ for Bayesian tracking. Location ambiguities observed for MLE case can be removed by Bayesian filtering.

GF techniques have accuracy limited by the grid spacing of $\Delta x = 0.5$m. The PF approach is thus proposed to improve the positioning performance without increasing the computational cost of the localization algorithm. The transition pdf has the same standard deviation as for GF. Fig. 9 compares three

[8]Clearly, initialization becomes critical in large areas with lower spatial density of nodes (and/or lower number of particles, considering PF). In case of node deployment along the perimeter, the location pdf could be initialized uniformly along the boundary or, better, concentrated around the access points of the considered area (doors or main paths, etc.).

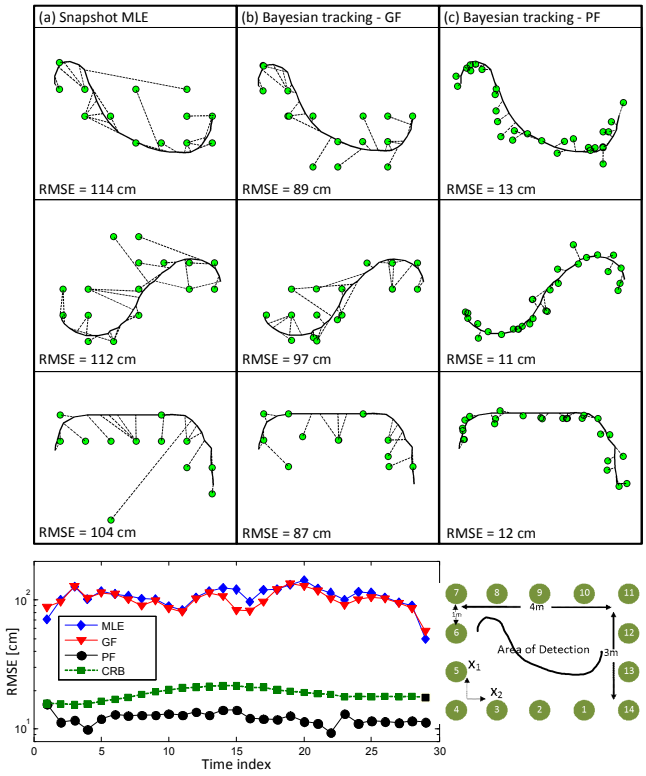

Fig. 9. Top figure. Examples of location trajectories (solid lines) and related estimates (markers). From left to right: MLE, GF and PF based Bayesian tracking. Dashed lines connecting the true and estimated positions highlight the localization errors. The RMSE averaged over the trajectory is indicated for each case. Bottom figure. RMSE and CRB performance as a function of the position along the corresponding trajectory (indicated in the sub-figure)

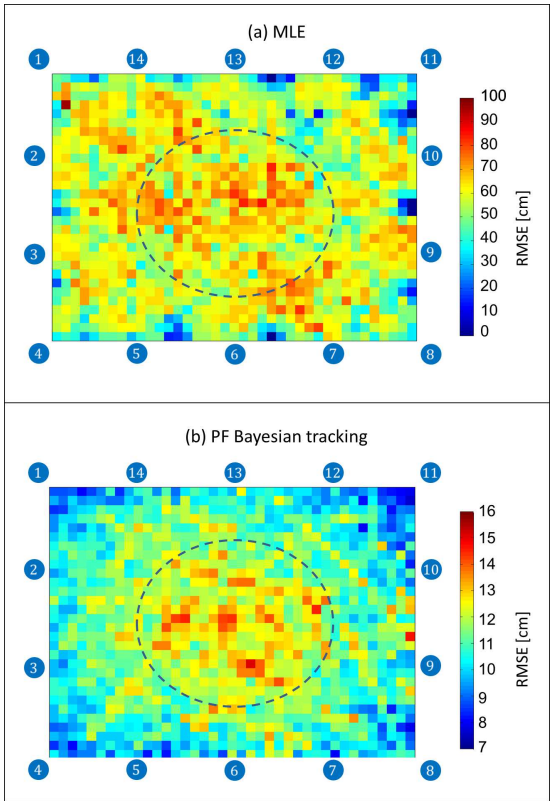

Fig. 10. RMSE for MLE (a) PF Bayesian tracking (b) as a function of the target position within the detection area X.

true reference target trajectories examples (solid line) with the estimated ones (markers) obtained by MLE (Fig. 9-(a)), MMSE GF-based tracking (Fig. 9-(b)) and MMSE PF-based tracking with 60 particles (Fig. 9-(c)). The localization errors can be appreciated by looking at the dashed lines that connect the true and the estimated positions. The RMSE of the location estimate averaged over the trajectory is also indicated for each case. It can be seen that the MLE performance is affected by false-localization problems that are especially higher in the center of the detection area, causing an average localization error of approximately 1m. A main limiting factor for the snapshot MLE is the limited spatial accuracy of the pairwise location measurements. Using the grid-based sampling, the MMSE tracking is shown to reduce the average error of about 10-20cm compared to MLE. However, an error floor is observed due to the fixed grid spacing: this error can be eliminated by the use of PF. This latter approach reduces the average RMSE to a value that is comparable with the size of the target (10-20cm). In Fig. 9 at bottom we show now the RMSE and the CRB (see Sect. V-C) performance as a function of the position corresponding to the trajectory indicated in the sub-figure (on the right). It can be noticed that the PF estimate greatly outperforms the MLE. In the considered case, the PF accuracy can actually outperform the CRB as the conventional CRB does not take into account the a-priori information that comes from the target motion.

In Fig. 10 the RMSE of the location estimate is shown as a function of the target position for both MLE and PF tracking. To evaluate the accuracy over a wider set of positions, a trajectory going along a regular grid of 10cm spacing and covering the whole space (back and forth, for a total of 2400 positions) has been generated. The corresponding RSS observations $\mathbf{s}_t$ and the likelihood function $p(\mathbf{s}_t|\mathbf{x}_t)$ are modeled as in (10). Performances have been averaged over 50 realizations of measurements. As expected the ML performance is above the CRB. On the other hand, the PF accuracy could outperform the CRB, as the conventional CRB does not consider the a-priori information. As also observed for the CRB analysis, the maximum positioning accuracy is located at the boundary of the detection area while the minimum is confined in the center now with RMSE= 14-16cm.

E. Localization for ambient-intelligence services with non-regular deployment in mixed LOS/NLOS environments

In this section we show a preliminary experiment that highlights the potential of the proposed system in more practical scenarios. The selected scenario, depicted in the top plot of Fig. 11, consists of a mixed LOS/NLOS environment with multiple rooms and corridors, characterized by different kinds of furniture. The radio devices are now deployed at strategic positions to guarantee connectivity, while the network protocol allows for the coexistence of two personal area network (PAN) coordinators simultaneously collecting the RSS measurements (from two sub-networks). Each node communicates with the

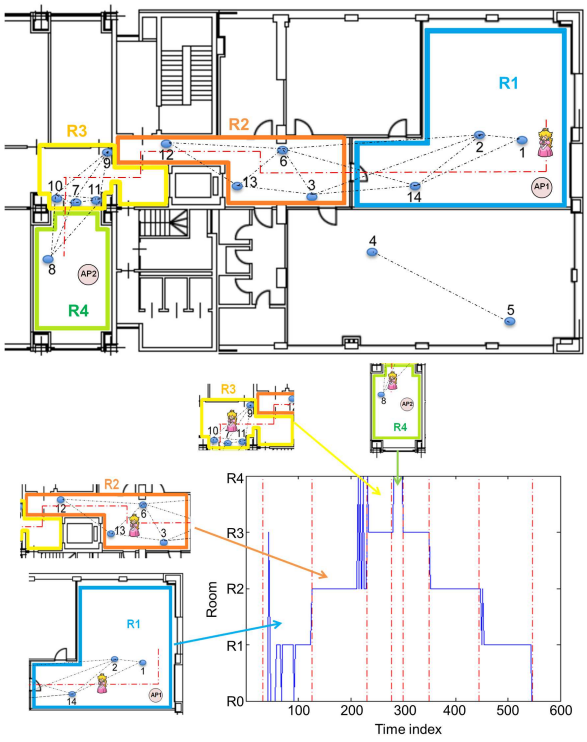

Fig. 11. Localization tests in a mixed LOS/NLOS environment with non-regular network deployment. The target area is divided in four areas/rooms (top) and MLE localization is used for room localization (bottom).

respective coordinator and overhears the messages of the adjacent devices (from which the RSS can be estimated).

As shown in Fig. 11, the radio devices are deployed in four different areas/rooms (labeled R1-R4 and highlighted by different colors). The mobile target walks along the trajectory in outward and return starting from room R1. The system is designed to support ambient intelligence (i.e., assisted living) services [29] by locating the target in the different rooms while moving across them. Preliminary estimation results based on the MLE technique are shown at the bottom of Fig. 11. Despite some false localizations, the system can detect and localize the target traversing each room. The estimation accuracy is lower than in previous experiments but it reasonably fits with the application requirements.

VI. Concluding Remarks

Device-free localization can be used to track objects or people moving in areas covered by a cooperative wireless network. In this paper a stochastic log-normal RSS model has been proposed to describe the fading effects caused by the object/human movement in both indoor and outdoor environments. In case of target presence the measured RSS is subject to a perturbation that depends on the specific position and affects both the average path-loss and the degree of fading fluctuations. The increase of path-loss and power fluctuation have been evaluated analytically based on the theory of diffraction. This allows to avoid time-consuming link-by-link calibration - mandatory for conventional tomographic or non-parametric fingerprinting methods - requiring the tuning of only few model parameters: the system can be therefore implemented, with minimal software adaptation, on top of existing wireless network standards supporting short-range device-to-device communication (WiFi/ZigBee/LTE-Direct) and easily integrated with RSS-based active localization systems. The model, combined with target motion prediction, has been used to cast the localization problem into the framework of Bayesian estimation. Fundamental limits to the positioning accuracy have been evaluated based on the analysis of the Cramer-Rao bound. The use of PF Bayesian tracking has been shown to provide an improved accuracy and it can thus be exploited to overcome the limits of positioning based on snapshot measurements, particularly in areas subject to reduced sensitivity. Further developments will be the extension to multiple targets, the integration with aggregate mobility models (e.g., for pedestrian flow tracking) and the implementation of more scalable partial/fully decentralized estimation schemes to support context aware people activity recognition. Integration of passive and active localization is also a new direction of research. Preliminary experiments show that the combined use of Bayesian localization and particle filtering allows dual target tracking with minimal complexity increase.

VII. Appendix

The electric field $E_1(\mathbf{x}_t,\theta_t)$ measured at the receiver may be interpreted as generated by a virtual array of Huygen sources located in the plane (x,z) of the target at distance d from the receiver. Considering a single infinitely small target element of area $dS = dxdz$ located at position (x_i,z_i) in the plane and at distance[9] $q_\ell(\mathbf{x}_t)$ from the transmitter, the received electric field $E_1(\mathbf{x}_t,\theta_t) = E_0 - dE_1(\mathbf{x}_t,\theta_t)$ is subject to a loss dE_1 compared to the energy E_0 that would be observed without the target. The electric field E_1 can be approximated[10] assuming that $\max\{|x_i|,|z_i|\} \ll \min\{q_\ell(\mathbf{x}_t),[d_\ell - q_\ell(\mathbf{x}_t)]\}$ and according to the following equation

$$E_1(\mathbf{x}_t,\theta_t) \simeq E_0 - j\frac{E_0}{r_\ell^2(\mathbf{x}_t)}\exp\left[\frac{-j\pi\left(x_i^2+z_i^2\right)}{r_\ell^2(\mathbf{x}_t)}\right]dxdz \tag{17}$$

where $r_\ell(\mathbf{x}_t)$ is defined in (6). Based on (17), the overall field loss $|E_1(\mathbf{x}_t,\theta_t)/E_0|$, for an object located at same distance $q_\ell(\mathbf{x}_t)$ from the transmitter and covering now all the positions $(x,z)\in\mathcal{R}_{\mathbf{x}_t,\theta_t}$, can be written as

$$\left|\frac{E_1(\mathbf{x}_t,\theta_t)}{E_0}\right| \simeq 1 - \int_{(x,z)\in\mathcal{R}_{\mathbf{x}_t,\theta_t}} dE_1(\mathbf{x}_t,\theta_t)dxdz =$$

$$= \frac{1}{2}\left|2 - j\int_{-\infty}^{\frac{\sqrt{2}b_z}{r_\ell(\mathbf{x}_t)}}\int_{-\frac{\sqrt{2}b(\theta_t)}{r_\ell(\mathbf{x}_t)}}^{\frac{\sqrt{2}b(\theta_t)}{r_\ell(\mathbf{x}_t)}}\exp\left[-j\pi\frac{s_1^2+s_2^2}{2}\right]ds_1ds_2\right|,$$

where we used the substitutions $s_1 = \sqrt{2}z/r_\ell(\mathbf{x}_t)$ and $s_2 = \sqrt{2}x/r_\ell(\mathbf{x}_t)$, while $b(\theta_t) = b_xb_y\left[\sqrt{b_x^2\cos^2(\theta_t)+b_y^2\sin^2(\theta_t)}\right]^{-1}$ measures the lateral section of the obstruction (acting as a knife-edge object) for random orientation $\theta_t \sim \mathrm{U}[-\pi,\pi]$. Using the

[9] measured along the ground rather than along the direct wave.

[10] as far as the target is confined within the first Fresnel volume.

approximation valid for $b_z \gg \max\{b(\theta_t), r_\ell(\mathbf{x}_t)\}$, and since $\lim_{A\to\infty}\int_{-\infty}^{A}\exp[-j\pi s_1^2/2]ds_1 = 1-j$ the energy loss can be simplified as

$$\left|\frac{E_1(\mathbf{x}_t,\theta_t)}{E_0}\right| \approx \left|(1+j)\int_{\sqrt{2}b(\theta_t)/r_\ell(\mathbf{x}_t)}^{+\infty}\exp\left[\frac{-j\pi s^2}{2}\right]ds\right| \tag{19}$$

Using an asymptotic expansion [30] for the integrals in the form $\int_0^x \exp\left[-j\pi\frac{x^2}{2}\right]dx \approx \frac{1}{2}+\frac{1}{\pi x}\sin(\frac{1}{2}\pi x^2) - j\left[\frac{1}{2}-\frac{1}{\pi x}\cos(\frac{1}{2}\pi x^2)\right]$ valid for large enough x, the energy loss (19) scales as

$$\left|\frac{E_1(\mathbf{x}_t,\theta_t)}{E_0}\right| \approx \frac{1}{\pi}\times\frac{r_\ell(\mathbf{x}_t)}{b(\theta_t)}. \tag{20}$$

The target-induced average attenuation $\Delta h_\ell(\mathbf{x}_t) = \mathrm{E}_{\theta_t}[|E_0/E_1|^2\,|_{\mathrm{dB}}] + \Delta h_0$ is approximated as

$$\Delta h_\ell(\mathbf{x}_t) \simeq \mathrm{E}_{\theta_t}\left[\left|\frac{E_0}{E_1(\mathbf{x}_t,\theta_t)}\right|^2\right]\Bigg|_{\mathrm{dB}} + \Delta h_0. \tag{21}$$

being $\mathrm{E}_{\theta_t}[|E_0/E_1|^2\,|_{\mathrm{dB}}] \le \mathrm{E}_{\theta_t}\left[|E_0/E_1|^2\right]|_{\mathrm{dB}}$ from Jensen inequality. The average term $\mathrm{E}_{\theta_t}\left[|E_0/E_1|^2\right]$ can be simplified by considering the lateral section $b(\theta_t)$ of the obstruction only for the azimuths $\theta_t = 0$ and $\theta_t = \pi/2$ assumed as equiprobable (see Fig. 2). We thus redefine the random variable $b(\theta_t)$ as: $b(\theta_t) = b(\theta_t)|_{\theta_t=0} = b_x$ with probability 1/2 and $b(\theta_t) = b(\theta_t)|_{\theta_t=\pi/2} = b_y$ with probability 1/2. We get:

$$\mathrm{E}_{\theta_t}\left[\left|\frac{E_0}{E_1(\mathbf{x}_t,\theta_t)}\right|^2\right] \simeq \frac{\pi^2}{r_\ell^2(\mathbf{x}_t)}\frac{1}{2\pi}\int_{-\pi}^{\pi}b^2(\theta_t)d\theta_t \simeq \gamma_1\frac{b_x^2+b_y^2}{r_\ell^2(\mathbf{x}_t)}, \tag{22}$$

with $\gamma_1 = \pi^2/2$. Using the same approximation, the standard deviation term is

$$\mathrm{std}_{\theta_t}\left[\left|\frac{E_0}{E_1(\mathbf{x}_t,\theta_t)}\right|^2\right] \simeq \gamma_1\frac{b_x^2-b_y^2}{r_\ell^2(\mathbf{x}_t)} \tag{23}$$

while the additional deviation $\Delta\sigma_\ell(\mathbf{x}_t)$ is computed as

$$\Delta\sigma_\ell(\mathbf{x}_t) \simeq \mathrm{std}_{\theta_t}\left[\left|\frac{E_0}{E_1(\mathbf{x}_t,\theta_t)}\right|^2\right]\Bigg|_{dB} + \Delta\sigma_0. \tag{24}$$

In Sect. III.C, it has been observed experimentally that the impact of the two approximations (21) and (22) is marginal for the considered scenarios.

REFERENCES

[1] N. Patwari, et al., "Locating the nodes: cooperative localization in wireless sensor networks," IEEE Signal Processing Mag., vol. 22, no. 4, pp. 54-69, July 2005.

[2] M. Youssef, M. Mah, A. Agrawala, "Challenges: device-free passive localization for wireless environments," Proc. ACM Int. Conf. on Mobile Computing and Networking (MobiCom), Montreal, Canada, Sept. 2007, pp. 222-229.

[3] A. Tang, Q. J. Gu, M.C. Chang, "CMOS receivers for active and passive mm-wave imaging," IEEE Commun. Mag., vol. 49, no. 10, pp. 190-198, Oct. 2011.

[4] S. Gezici, et al., "Localization via ultra-wideband radios: a look at positioning aspects for future sensor networks," IEEE Signal Processing Mag., vol. 22, no. 4, pp. 70–84, July 2005.

[5] J. Wilson, N. Patwari, "Radio tomographic imaging with wireless networks," IEEE Trans. on Mobile Comp., vol. 9 no. 5, pp. 621-632, May 2010.

[6] M. Nicoli, C. Morelli, V. Rampa, "A jump Markov particle filter for localization of moving terminals in multipath indoor scenarios," IEEE Trans. Signal Processing, vol. 56, no. 8, pp. 3801-3809, Aug. 2008.

[7] M. Nicoli, D. Fontanella, "Fundamental Performance Limits of TOA-based Cooperative Localization," Proc. IEEE Int. Conf. on Commun. Workshops (ICC), pp. 1-5, Dresden, 14-18 June 2009.

[8] P. Misra, N. Ahmed, S. Jha, "An empirical study of asymmetry in low-power wireless links," IEEE Commun. Mag., vol. 50, no. 7, pp. 137-146, July 2012.

[9] P. K. Chong, et al., "Wind-blown foliage and human induced fading in ground-surface narrowband communications," IEEE Trans. on Vehicular Technology, vol. 60, no. 4, pp. 1326-1336, May 2011.

[10] A.J. Coulson, A.G. Williamson, and R.G. Vaughan, "A statistical basis for lognormal shadowing effects in multipath fading channels," IEEE Trans. Veh. Technol., vol. 46, no. 4, pp. 494–502, April 1998.

[11] D.J.Y. Lee, W.C.Y. Lee, "Propagation prediction in and through buildings," IEEE Trans. on Vehicular Technology, vol. 49, no. 5, pp. 1529-1533, Sept. 2000.

[12] K. Srinivasan, P. Levis, "RSSI is Under Appreciated," Proc. of the Third Workshop on Embedded Networked Sensors (EmNets), 2006.

[13] M. Ghaddar, L. Talbi and T.A. Denidni, "Human body modeling for prediction of effect of people on indoor propagation channel," IEEE Electronic Letters, vol. 40, no. 25, pp. 1827-1835, Dec. 2004.

[14] M. Cheffena, "Physical-statistical channel model for signal effect by moving human bodies," EURASIP Journal on Wireless Communications and Networking, no. 77, pp. 1-13, Jan. 2012.

[15] Y.I. Nechayev, P.S. Hall, Z.H. Hu, "Characterisation of narrowband communication channels on the human body at 2.45 GHz," IET Microw. Antennas Propag., vol. 4, no. 6, pp. 722-732, June 2010.

[16] G. E. Athanasiadou, "Incorporating the Fresnel zone theory in ray tracing for propagation modelling of fixed wireless access channels," Proc. of IEEE Int. Symp. on Personal, Indoor and Mobile Radio Communications (PIMRC), Sept. 2007, pp. 3-7.

[17] A. Eleryan, M. Elsabagh, M. Youssef, "Synthetic generation of radio maps for device-free passive localization," Proc. IEEE Global Commun. Conf. (GLOBECOM), Houston, pp. 1-5, Dec. 2011.

[18] S. Savazzi, M. Nicoli, M. Riva, "Radio Imaging by Cooperative Wireless Network: Localization Algorithms and Experiments," IEEE Wireless Communications and Networking Conference (WCNC), Paris, 1-4 April 2012, pp. 2357-2361.

[19] H. Mokhtaru, P. Lazaridis, "Comparative study of lateral profile knife-edge diffraction and ray tracing technique using GTD in urban environment," IEEE Trans. on Vehicular Technology, vol. 48, no. 1, pp. 255-261, Jan. 1999.

[20] A. Nyuli, B. Szekeres, "An improved method for calculating the diffraction loss of natural and man-made obstacles," Proc. of IEEE Int. Symp. on Personal, Indoor and Mobile Radio Communications (PIMRC), Oct. 1992, pp. 426-430.

[21] C. L. Giovanelli, "An analysis of simplified solutions for multiple knife-edge diffraction," IEEE Trans. on Antennas and Propagation, vol. 32, no. 3, pp. 297-301, Mar. 1984.

[22] C. Morelli, M. Nicoli, V. Rampa, U. Spagnolini, "Hidden Markov models for radio localization in mixed LOS/NLOS conditions," IEEE Trans. Signal Processing, vol. 55, no. 4, pp. 1525-1542, April 2007.

[23] F. Gustafsson, F. Gunnarsson, "Mobile positioning using wireless networks," IEEE Signal Process. Mag., vol. 22, no. 4, pp. 41-53, July 2005.

[24] M. S. Arulampalam, et al. "A tutorial on particle filters for online nonlinear/non-Gaussian Bayesian tracking," IEEE Trans. Signal Proc., vol. 50, no. 2, pp. 174-188, Feb. 2002.

[25] L. R. Rabiner, "A Tutorial on Hidden Markov Models and Selected Applications in Speech Recognition," Proc. of the IEEE, vol. 77, no. 2, pp. 257-286, Feb. 1989.

[26] S. Kay, Fundamentals of Statistical Signal Processing, Volume I: Estimation Theory, Prentice Hall, 1993.

[27] Datasheet CC2420, 2.4 GHz IEEE 802.15.4 ZigBee-ready RF Transceiver, Mar. 2007.

[28] E. Tovar, F. Vasques, "Real-time fieldbus communications using Profibus networks," IEEE Trans. on Industrial Electronics, vol. 46, no. 6, pp. 1241-1251, Dec. 1999.

[29] D. J. Cooky, J. C. Augustoz, and V. R. Jakkula, "Ambient Intelligence: technologies, applications, and opportunities," Pervasive and Mobile Computing, vol. 5, no. 4, pp. 277-298, August 2009.

[30] M. Abramovitz, I. A. Stegun, "Handbook of mathematical functions," Applied mathematics series 55, Dec. 1972.